ChemCatChem

Research Article
doi.org/10.1002/cctc.202300671

Chemistry Europe
European Chemical
Societies Publishing

www.chemcatchem.org

First-Principles Microkinetic Study of the Catalytic Hydrodeoxygenation of Guaiacol on Transition Metal Surfaces

Fabian Morteo-Flores,[a] Max Quayle,[a] Antoni Salom-Català,[a] Marc Pera-Titus,[a] and Alberto Roldan Martinez*[a]

The mechanism behind the hydrodeoxygenation (HDO) of guaiacol on Co(0001), Ni(111), Cu(111), Pd(111), and Pt(111) was investigated by constructing a first-principles microkinetic model from density functional theory (DFT) models for 68 possible intermediates over each surface. We report that the most energetically favorable pathway for this process is the demethylation of guaiacol to catechol over Ni(111), which exhibits highly desirable deoxygenation and hydrogenation kinetics at industrial temperatures. Guaiacol readily undergoes hydrogenation over Pt(111) and Pd(111), but the products exhibit slow desorption from the surfaces at standard operation temperatures. Furthermore, the deoxygenation pathway is hindered by the high energy barrier associated with the scission of the C_{alkyl}—O bond.

Introduction

As the Earth's oil and natural gas reservoirs continue to dwindle,[1] it is becoming increasingly critical that the chemical industry moves to a circular economy. One of the most promising renewable feedstocks is bio-oil, which is a liquid fuel generated from the pyrolysis of lignocellulosic biomass. In order to increase the energy density of bio-oil and to depolymerize bulky lignin subunits in solution into small and more industrially applicable monomers, raw bio-oil must undergo catalytic upgrading.[2] Hydrodeoxygenation (HDO) is a common strategy to improve the quality of raw bio-oil, a process in which oxygen heteroatoms are removed from the lignin subunits as water; ideally, with as little cracking of the deoxygenated compounds as possible.[3,4] HDO is typically performed in two stages.[5] In the first stage, methoxy phenols, esters and ethers in the bio-oil are converted into simple phenols and furans. However, small concentrations of ketones and carboxylic acids will remain in solution. In the second stage, where hydrogen gas is introduced into the reactor, thus ensuring that HDO is carried out to completion. Phenols, furans and carbonyls are then converted into their deoxygenated analogues, increasing the energy density of the fuel by as much as 46 MJ kg^{-1}.[6]

Owing to the importance of HDO in catalysis and the energy sector, it is crucial that the mechanistic chemistry behind this strategic reaction is properly understood. Using atomistic simulations, computational chemists can model the individual elementary steps of bio-oil HDO.[7] The data from these simulations can then assist synthetic chemists in the promotion of new catalytic pathways. Due to the sheer number of different lignin subunits that may be present in a given bio-oil sample, simulations must be restricted to a handful of representative model compounds out of practical necessity. In recent years, guaiacol (1-hydroxy-2-methoxybenzene, GUA) has been a popular model compound for computational bio-oil research.[7–10] Like one-third of the most common lignin subunits in phenolic bio-oil fractions,[11] guaiacol has two different oxygen functional groups branching from a benzene ring; in this case, an alcohol group and a methoxy group in an ortho conformation. Guaiacol and its derivatives are common in bio-oil and raw biomass,[2,12] and can be readily converted into useful aromatic compounds such as phenol and benzene. Because of the relative ease with which guaiacol can be converted into high-value feedstocks makes it a particularly salient model compound for catalytic processes.

As shown in Scheme 1, guaiacol HDO can proceed through three initial pathways: dehydroxylation to anisole (ANI) (**P1**), demethoxylation to phenol (PHE) (**P2**), and demethylation to catechol (CAT) (**P3**).[13–15] From here, the reaction can proceed through one of several pathways to benzene (BEN). In the direct deoxygenation (**P4**) and demethylation (**P5**) pathways, catechol and anisole are converted into phenol. Benzene can then be produced both from the demethoxylation of anisole (**P6**) and the hydrogenolysis of phenol (**P7**). A comprehensive table of predicted intermediates for each reaction pathway (**S1**-**S68**) is given in the Supporting Information.

DFT calculations can be validated by comparing derived microkinetic modelling techniques with experimental kinetics data. The results of these calculations can then aid chemical

[a] *Dr. F. Morteo-Flores, M. Quayle, Dr. A. Salom-Català, Prof. M. Pera-Titus,*
Dr. A. R. Martinez
Cardiff Catalysis Institute
School of Chemistry
Cardiff University
Main Building, Park Place
Cardiff, CF10 3AT (UK)
E-mail: roldanmartineza@cardiff.ac.uk
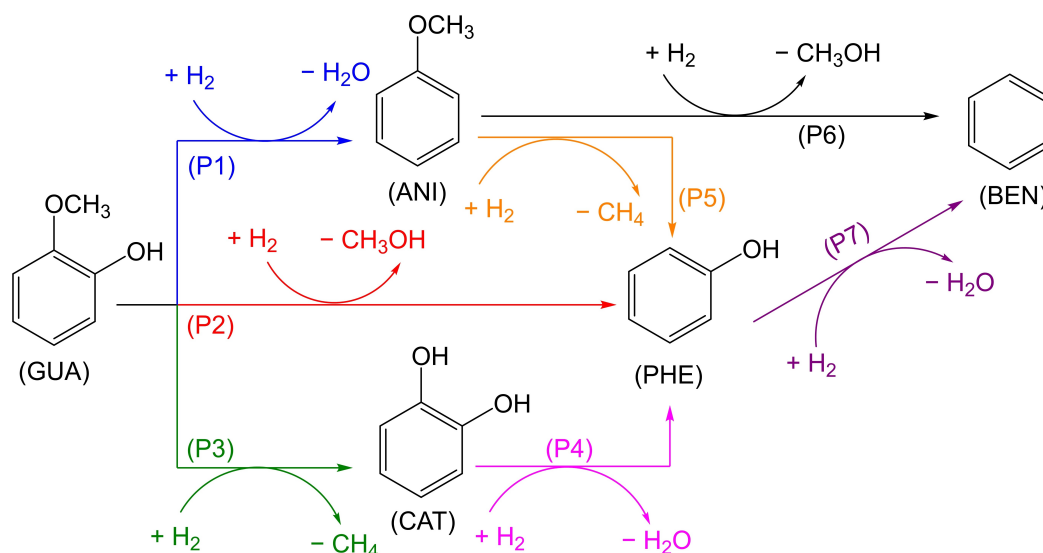
Scheme 1. Potential reaction pathways for the hydrodeoxygenation of guaiacol (GUA) to benzene (BEN).[7]

engineers and experimentalists in deducing the conditions and catalysts necessary for optimum yield and selectivity. For instance, Nimmanwudipong et al.[14] used microkinetic modelling to study the conversion of guaiacol into phenol and anisole on Pt/γ-Al$_2$O$_3$ in the presence of H$_2$ at 573 K. The kinetic data from this work confirmed that the selectivity of guaiacol HDO is positively correlated to both an increase in H$_2$ partial pressure and a decrease in the temperature of the reactor. Another microkinetic study by Bjelić et al.[16] on the HDO of eugenol reported that the hydrogenation/deoxygenation ratio of the starting material was the highest over Pd/C and the lowest over Ru/C, and that deoxygenation could be promoted by increasing the temperature.

Following our previous work on the mechanistic chemistry of guaiacol HDO through DFT,[7] we employed microkinetic modelling to gain a deeper understanding of how the kinetics of the individual steps can be affected with by adjusting the reaction conditions over a range of transition metal catalysts.

Computational Details

DFT Calculations

Spin-polarized DFT calculations were performed using the Vienna Ab-Initio Simulation Package (VASP)[17,18] for a range of guaiacol HDO mechanistic pathways over slab models of Co(0001), Ni(111), Cu(111), Pd(111), and Pt(111). Following the methodology of our previous work on guaiacol HDO,[7] the exchange-correlation contributions were calculated within the constraints of the generalized gradient approximation (GGA) using the revised Perdew-Burke-Ernzerhof (RPBE) functional.[19] Each slab consisted of a 6×6 supercell with five atomic layers and a 15 Å vacuum layer perpendicular to the surface. The top two layers of each slab were relaxed, and the rest were frozen after the initialization step. A kinetic energy cut-off value of 550 eV was chosen for the valence electron plane-wave basis set, and long-range dispersion interactions were accounted for by utilizing the DFT-D3 method

developed by Grimme et al.[20] The Brillouin zone was sampled with a 3×3×1 Monkhorst-Pack grid,[21] and partial occupancies were determined using the first-order Methfessel-Paxton method[22] with a smearing width of 0.2 eV. All transition states were identified by using the climbing-image nudged elastic band method (CI-NEB)[23] in tandem with the improved dimer method, which were then verified with vibrational analysis. More information on the confirmations of the adsorbates and the construction of the slab models is given in the Supporting Information.

Microkinetic Modelling

We calculated the thermodynamic properties (entropy, specific heat, enthalpy, and free energy) of each elementary step as functions of temperature.[24] Translational, rotational, vibrational, electronic and nuclear contributions to the partition functions were considered as described and validated elsewhere.[25–28] Following the assumptions of transition states theory, the rate constants (k) for each elementary step were determined using the Eyring-Polanyi equation (Eq. 1):[29]

$$k = \frac{k_B T}{h} \cdot \frac{q_{TS}}{q_{IS}} \cdot e^{\frac{-\Delta G_a}{k_B T}}$$

(1)

where k_B is the Boltzmann constant, h is Planck's constant, ΔG_a is the activation free energy, and q_{IS} and q_{TS} are the partition functions of the initial state and the transition state, respectively. A batch reactor microkinetic model was then employed using an in-house code.[26,30,31] This model makes three main assumptions: (1) each site on the surface is identical; (2) the species adsorb randomly; and (3) adsorbates do not interact laterally once bound to the surface, which can be accounted for by keeping the surface coverage low. The rates of adsorption (r_{ads}) and their respective rate constants (k_{ads}) were calculated using the Hertz-Knudsen equations (Eqs. 2–3):[32]

$$r_{ads} = k_{ads} \cdot P_X \cdot \theta*$$

(2)

$$k_{ads} = \frac{A}{\sqrt{2\pi m_X k_B T}} \cdot S_o$$

(3)

ChemCatChem

Research Article
doi.org/10.1002/cctc.202300671

Chemistry
Europe
European Chemical
Societies Publishing

where P_X is the partial pressure of species X in the batch reactor, θ_* is the fraction of free sites on the surface, A is the surface area occupied by X, and m_X is the mass of a single molecule of X. The sticking coefficient (S_o), defined as the fraction of collisions leading to molecular adsorption from the gas phase, was calculated as follows (Eq. 4):

$$S_o = \frac{q_{vib}^{TS}}{q_{trans}^{2D} \cdot q_{rot}^{gas} \cdot q_{vib}^{gas}} \cdot e^{\frac{-\Delta G}{k_B T}} \qquad (4)$$

where ΔG is the change in the free energy of the system. q_{vib}^{TS}, q_{trans}^{2D}, q_{rot}^{gas}, and q_{vib}^{gas} are the respective partition functions for vibration of the adsorbate in the transition state, translation across the surface in the 2D plane, rotation in the gas phase, and vibration in the gas phase, respectively. It should be stressed that when a molecule moves perpendicular to the surface towards a transition state, translations and rotations are frustrated and can subsequently be neglected. As such, the partition function in the numerator of Equation 4 only contains the vibration term, q_{vib}^{TS}.

Following the experimental observations of Massoth et al. on the kinetics of hydrodeoxygenation reactions,[33] the elementary steps of guaiacol HDO were chosen to correspond to the expected intermediates of a Langmuir-Hinshelwood mechanism. The reaction begins with the adsorption of guaiacol and molecular hydrogen on neighboring surface sites. H_2 then dissociates on the metal surface and, through the hydrogenation of the co-adsorbed molecule, cleaves one of three potential bonds: the C_{aryl}—OH bond (**P1**), the C_{aryl}—OCH_3 bond (**P2**), or the O—CH_3 bond of the methoxy group (**P3**).

Results and Discussion

Optimizing the temperature of the reactor is a crucial step in industrial HDO to balance the adsorption of reactants on the surface and their capacity to surmount activation energies. For every combination of surface and adsorbate, S_o is known experimentally to tend exponentially to zero as the temperature increases.[34] At high temperatures, the internal energy of molecules in the gas phase is more significant than at low temperatures, thus making them less likely to stick to a surface upon collision or to remain adsorbed on it. Molecules already bound to the surface will be able to react with hydrogen adatoms at high temperatures, but the resulting competition between desorption and hydrogenation will inevitably result in lower catalytic activity.

Sticking Coefficients

Sticking coefficients (S_o) for catechol, anisole, guaiacol, and phenol were modeled over Co(0001), Ni(111), Cu(111), Pd(111), and Pt(111) surfaces. Figure 1 depicts the results as a function of temperature from 273 K to 1073 K.

As expected, all of the surfaces in Figure 1 show that S_o is at its the largest at lower temperatures. Due to the practical difficulties involved with accurately measuring S_o, experimental data on the sticking coefficients of guaiacol on individual transition metal surfaces are scarce. However, in an experimental investigation on the adsorption of phenol on Ni(111) and

Pt(111) surfaces by Carey et al.,[36] single crystal adsorption calorimetry confirmed that the temperature was inversely proportional to the probability of successful sticking of the substrate. Agrawal et al. used the same microkinetic model described in the Computational Details section, and found a good correlation with these results.[31] As the sticking coefficients of guaiacol on Co(0001), Cu(111), and Pd(111) are also at their highest at the lower end of the temperature range, we can reasonably predict that they will follow the trend verified for Ni(111) and Pt(111), and that catalysis will be at its optimum within this range.

Thermochemical Analysis

Scheme 2 shows the elementary steps of the dehydroxylation (**P1**), demethoxylation (**P2**), and demethylation (**P3**) pathways. Following Equations 1 and 4, Figure 2 shows the calculated activation (ΔG_a) and reaction (ΔG_r) free energies of the rate-determining steps of these pathways at 573 K, one of the most common temperatures for guaiacol HDO in industry.[37,38] Additional measurements of ΔG_a and ΔG_r between 273 K to 1073 K can be found in the Supporting Information (Tables B1–B5).

In this temperature range, the activation free energy associated with the cleavage of the C_{aryl}—OH bond (**S4**) is the lowest over Co(0001). Further hydrogenation of the cleaved intermediate to anisole (**S5**) is most thermodynamically favorable on Pt(111). The last step of the **P1** pathway is the formation of water from the cleaved hydroxy group (**S7**). At 573 K, **S7** is exothermic over Cu(111), Pt(111) and Pd(111), although only Pd(111) and Pt(111) show activation free energies of less than half an electronvolt. Our findings mirror the results of previous studies, in which guaiacol HDO over Ni(111), Co(0001) and Pt(111) did not display selectivity towards the dehydroxylation pathway at 573 K.[39–41] The high dissociation energy of the C_{aryl}—OH bond compared to the C_{aryl}—OCH_3 bond is the main limiting factor for anisole production over phenol and catechol. However, the dependency of the activation free energies on surface choice suggests that Pd(111) and Pt(111) can activate this bond.

The demethoxylation pathway (**P2**) starts with the hydrogenation of guaiacol, where the C_{aryl}—OCH_3 bond is cleaved to form phenol (**S12**); a step that is endothermic regardless of catalyst choice ($\Delta G_a \geq +1.30$ eV). The formation of phenol from the demethoxylated intermediate and atomic hydrogen (**S13**) is only favorable on Pt(111) and Pd(111). The hydrogenation of the cleaved methoxy group to methanol (**S15**) is exothermic over Pd(111) and Pt(111) for all temperatures. However, the large activation energy barrier of the C_{aryl}—OCH_3 scission step proved to be a limiting factor, as experimentally reported for Ni, Pt, and Co-catalyzed guaiacol HDO.[42,43]

The demethylation pathway (**P3**) begins with the scission of the C_{alkyl}—O bond (**S20**). This step is exothermic at 573 K, with Co(0001) having the highest free reaction energy ($\Delta G_r = -0.84$ eV). At 1073 K, step **S20** is particularly favorable over Pd(111). In contrast, the metals with the lowest activation free energies at 573 K are Ni(111) and Co(0001). The formation of
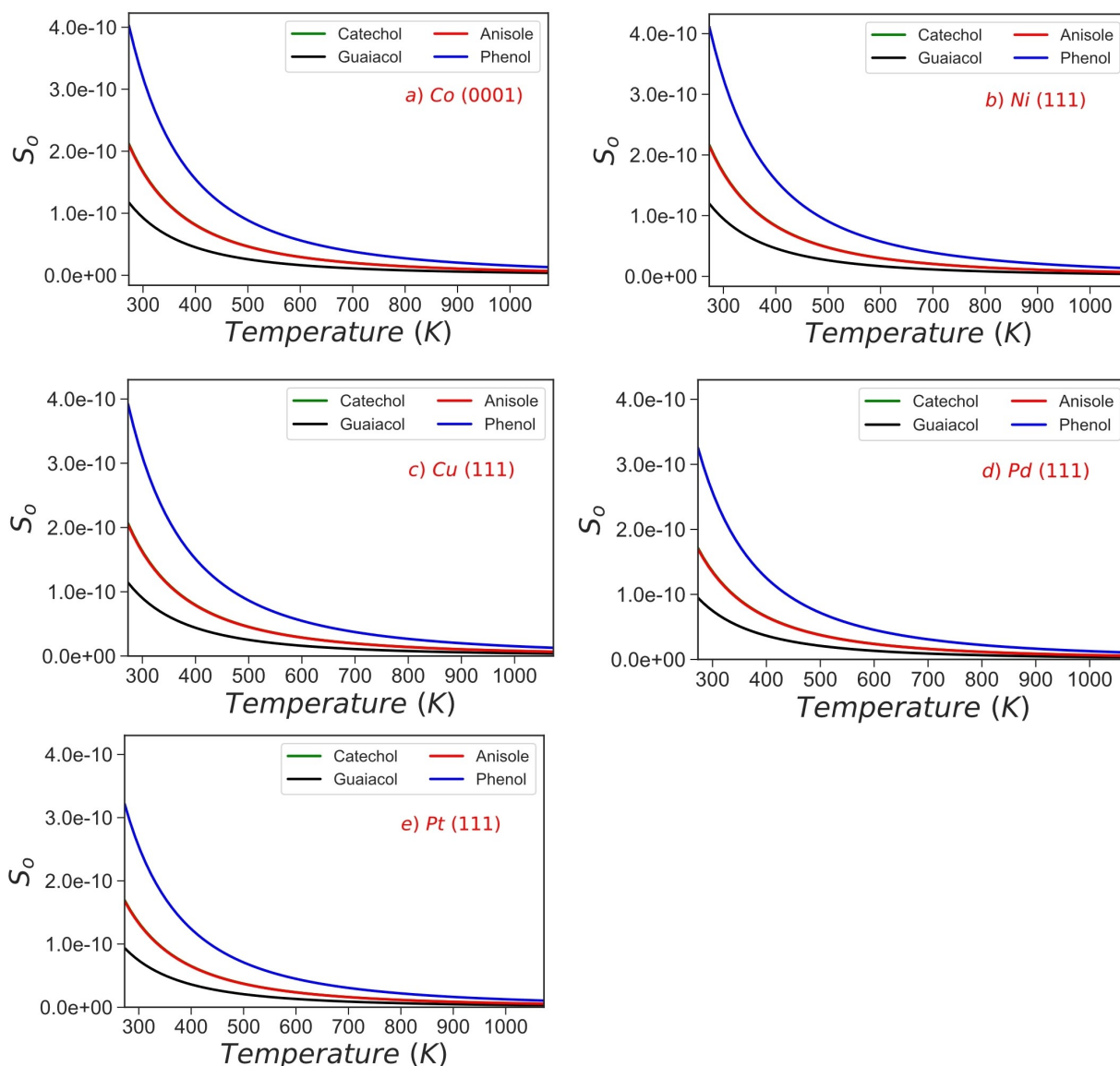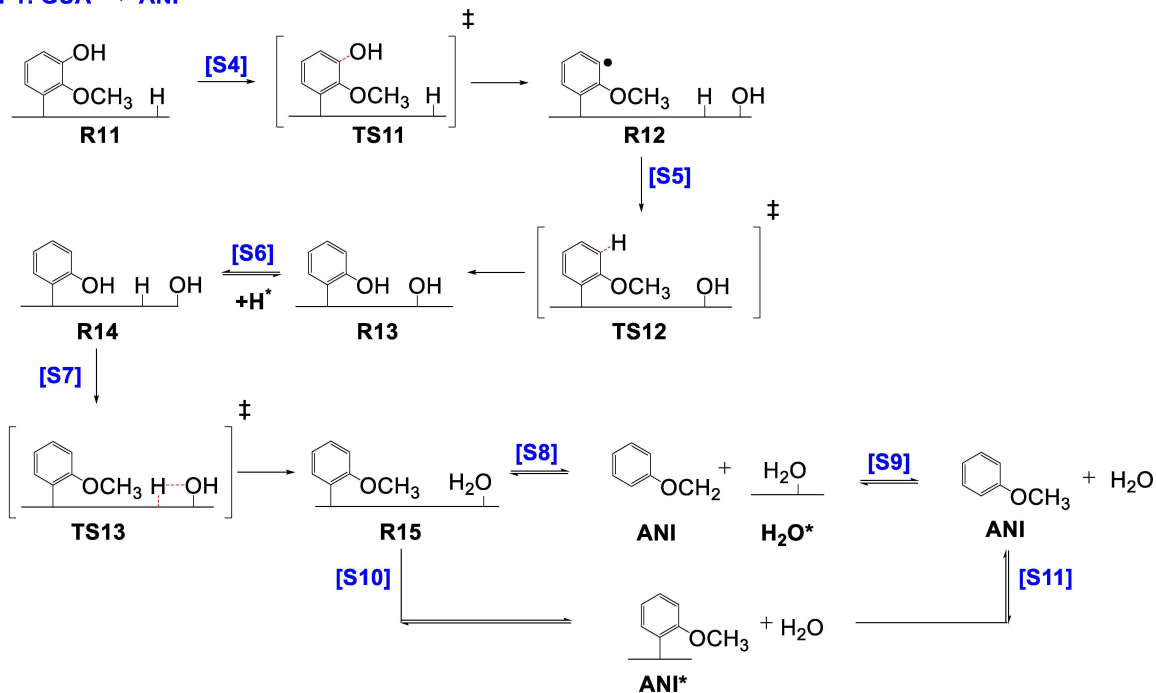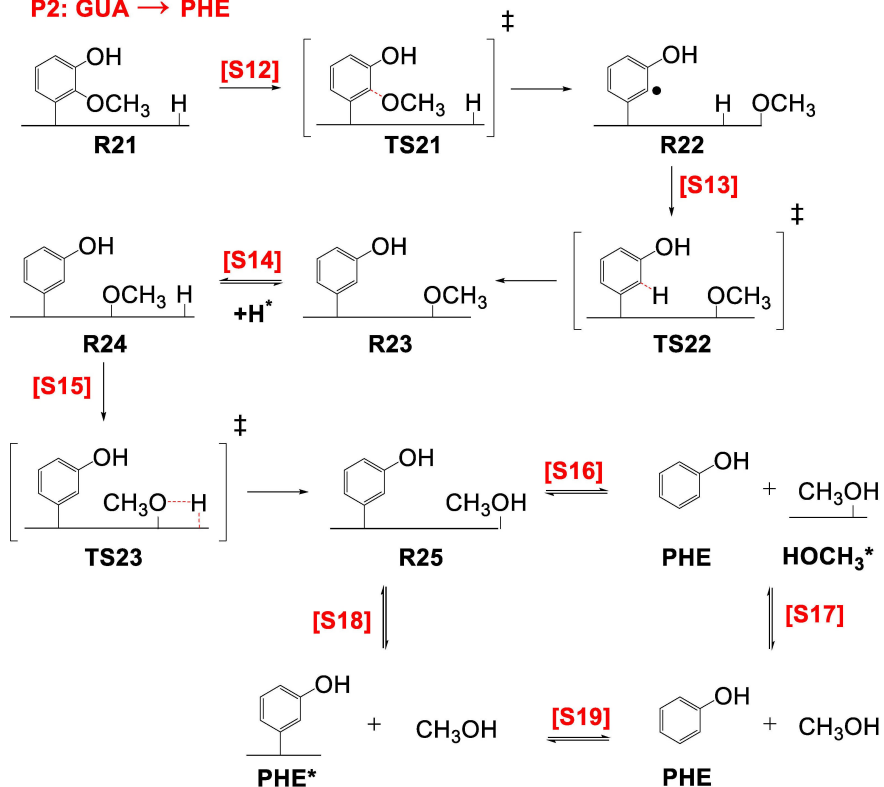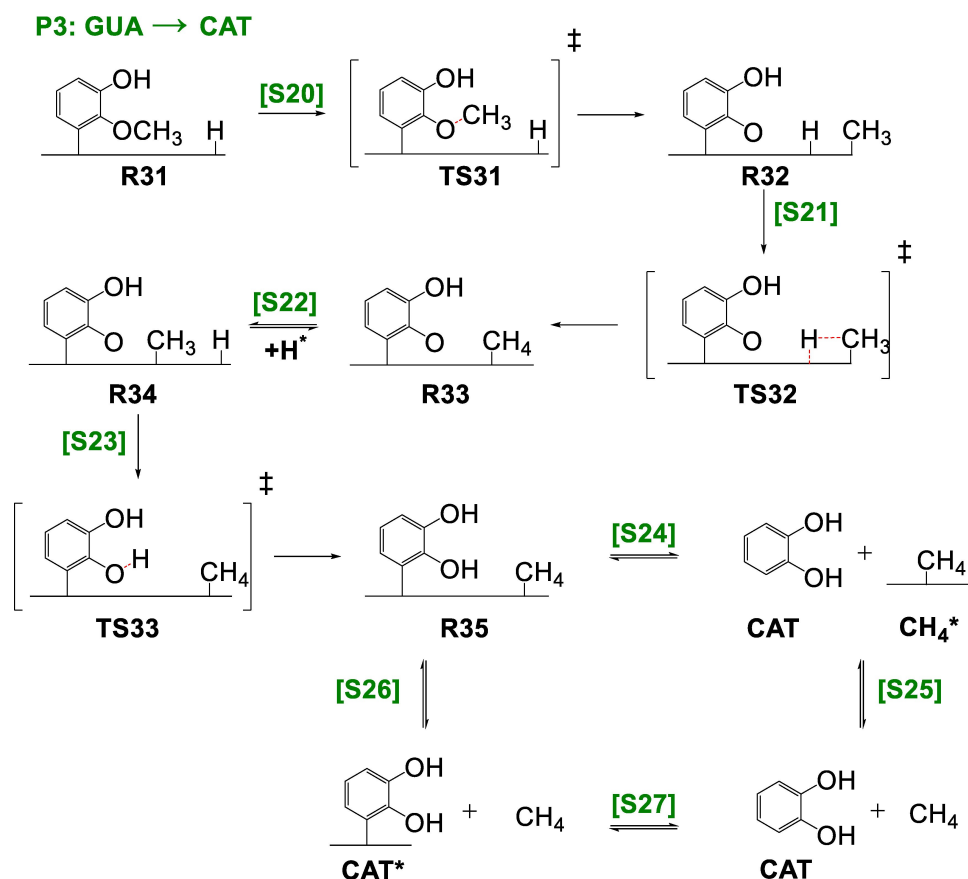
ChemCatChem

Research Article
doi.org/10.1002/cctc.202300671

**Chemistry
Europe**

European Chemical
Societies Publishing

Figure 1. Sticking coefficient (S_o) plots as a function of temperature for the adsorption of catechol, anisole, guaiacol, and phenol on a) Co(0001), b) Ni(111), c) Cu(111), d) Pd(111) and e) Pt(111). Due to the similar bonding conformations that anisole and catechol adopt in this temperature range on transition metal surfaces,[35] their respective sticking coefficients were almost identical. As a result, the sticking coefficient plots of anisole in red obscure the plots for catechol in green.

methane from the cleaved methyl group (**S21**) is most favorable over Pt(111) and Ni(111). Finally, for the final hydrogenation of the demethylated intermediate to catechol (**S23**), Ni(111) proves to be the most effective catalyst, with an activation energy of $\Delta G_a = +0.40$ eV at 573 K, which further decreases to $+0.17$ eV at 1073 K. Both Pt(111) and Pd(111) exhibit poor deoxygenation activity with high activation barriers and endothermic behavior, which can be attributed to guaiacol forming strong bonds with these surfaces. Based on these results, Ni(111) emerges as the best catalyst to promote the scission of the C_{alkyl}—O bond.

Following the demethylation of guaiacol to catechol (**P3**), the reaction can then proceed via the removal of the —OH groups from the adsorbate. The removal of one -OH group generates phenol (**P4**), and the removal of both generates

benzene (**P7**). Scheme 3 shows the elementary steps of these pathways, and Figure 3 shows the activation (ΔG_a) and reaction (ΔG_r) free energies of each step at 573 K. The scission of the first C_{aryl}—OH bond (**S31**) is hindered by a high activation energy barrier. Among the metals considered in this investigation, Co(0001) is the most favorable catalyst for this step. In contrast, direct deoxygenation is decidedly unfavorable over Pt(111) under the same conditions, with an activation free energy of over $+2.00$ eV. In agreement with experiment,[40,41] the hydrogenation of the dehydroxylated intermediate to phenol (**S32**) over Cu(111), Pt(111) and Pd(111) is exothermic at 573 K, with predominantly low activation free energies over Pt(111) and Pd(111) catalysts. Water formation (**S34**) is only exothermic over Cu(111), Pt(111) and Pd(111) at 573 K. Among the three metal surfaces, Pt(111) is by far the best catalyst for water formation

ChemCatChem

Research Article
doi.org/10.1002/cctc.202300671

**Chemistry
Europe**

European Chemical
Societies Publishing

P1: GUA → ANI

P2: GUA → PHE

ChemCatChem

Research Article
doi.org/10.1002/cctc.202300671

Chemistry Europe
European Chemical
Societies Publishing

Scheme 2. The elementary steps of dehydroxylation to anisole (**P1**, blue), demethoxylation to phenol (**P2**, red), and demethylation to catechol (**P3**, green).

under typical operation conditions ($\Delta G_a = +0.08$ eV). However, in practice, the availability of this pathway is expected to be blocked by the large activation energy barrier of **S31** ($\Delta G_a = +2.06$ eV).

The first step of **P7** (**S61**) has a high activation barrier at 573 K for all the metal surfaces ($\Delta G_a \geq +1.30$ eV). At this temperature, C_{aryl}–OH scission is only thermodynamically favorable over Co(0001). Subsequent hydrogenation to benzene (**S62**), however, is most thermodynamically favorable over Pd(111) and Pt(111), with relatively low activation energies over both surfaces. Like the water formation step in **P4** (**S32**), the formation of water from the hydroxy group (**S64**) is only exothermic over Cu(111), Pt(111) and Pd(111), with a particularly low activation energy over Pt(111) ($\Delta G_a = +0.16$ eV). It should be noted that the experimental work of Anton and Cadogan[43] on the formation of deuterated water over Pt(111) gives a substantially higher activation energy for this process between 373–723 K ($\Delta G_a = +0.70$ eV). While this value is lower than our calculated activation energies for any other metal in this investigation for step **S32** at 573 K, indicating a clear preference for Pt(111), it is half an electronvolt larger than any other calculated activation energies for Pt(111), and is roughly equal to the activation energies for step **S64** over Ni(111) and Pd(111). A DFT study by Karp et al.[44] on the energetics of deuterated water revealed that the enthalpy of formation of H_2O from adsorbed H and OH over Pt(111) is roughly 10%

lower than the enthalpy of formation of D_2O due to H/D isotope effects. As the same mechanism is expected to operate regardless of the isotopic distribution of the reagents, we can assume from the Evans-Polanyi principle[45] that this trend will also be present in the respective activation energies for H_2O and D_2O formation. Our model's omission of the effects of surface coverage and defects likely contributes to the underestimation of the activation energy for this step. The distribution of adsorbed hydrogen atoms, cleaved hydroxyl groups, and Pd atoms will be much less orderly on an experimental surface, and as such, we can reasonably expect that more energy will be needed for hydrogen atoms to migrate across the metal surface to the OH groups.

Microkinetics

To elucidate which catalyst is more active and selective for guaiacol HDO, we implemented the different mechanistic pathways (**P1**–**P7**) in microkinetic simulations. The rate constants (k) for the 68 elementary steps were calculated as a function of temperature. The partial pressure ratio of guaiacol and hydrogen gas was set at 1:5 for all microkinetic calculations. Figure 4 shows the rate constants of the rate limiting steps of guaiacol HDO on Co(0001), Ni(111), Cu(111), Pd(111) and Pt(111) at 573 K. Comprehensive tables of rate

ChemCatChem

Research Article
doi.org/10.1002/cctc.202300671

**Chemistry
Europe**

European Chemical
Societies Publishing

Figure 2. Activation free energies (ΔG_a) and reaction free energies (ΔG_r) of the elementary steps of dehydroxylation to anisole (**P1**, blue), demethoxylation to phenol (**P2**, red), and demethylation to catechol (**P3**, green) over each metal surface at 573 K.

constants and their associated pre-exponential factors (*A*) for all 68 steps can be found in the Supporting Information.

The C_{aryl}—OH scission (**S4**) rate constants for the dehydroxylation pathway are low at 573 K, following the decreasing order of Co(0001), Ni(111), Pt(111), Pd(111), and Cu(111). In the case of Ni(111) and Pd(111), the rate constants for the hydrogenation steps (**S5**, **S7**) are ten orders of magnitude larger than those for the C_{aryl}—OH scission step (**S4**). Similar trends are observed for the demethoxylation and demethylation steps (**S12**, **S13**, **S15**), which are favored over Co(0001) and Ni(111). It should be noted that the rate constant for C_{alkyl}—O bond scission during demethylation over Ni(111) is over twenty times larger than the rate constant over Co(0001)-catalyzed methoxylation. The sizable difference between the rate constants of the pathways' respective rate-limiting steps strongly indicates that, in the early stages of the reaction, Ni(111)-catalyzed demethylation (**P3**) is a more energetically favorable mechanistic

pathway for guaiacol HDO than Co(0001)-catalyzed methoxylation (**P2**).

The rate constant for the final hydrogenation step in **P3** to catechol (**S23**) is ten orders of magnitude larger for Ni(111) than that of any other metal in this investigation. However, the rate constant for C_{aryl}—OH bond scission (**S31**) in the direct deoxygenation pathway (**P4**) is five orders of magnitude larger over Co(0001) compared to Pt(111). It should also be noted that the rate constant at 573 K for water production (**S34**) is at its largest over Pt(111). These predictions agree with experimental observations that Pt(111) is a suitable catalyst for hydrogenation at 573 K, but a poor catalyst for deoxygenation at the same temperature.[16,46]

The hydrogenolysis of phenol to benzene (**P7**) is limited by the energy needed for C_{aryl}—OH bond scission (**S61**). The rate constant for this step is most prominent for Co(0001), followed by Ni(111), Cu(111), Pd(111) and Pt(111). However, the rate constant for the subsequent phenyl hydrogenation step (**S62**) is
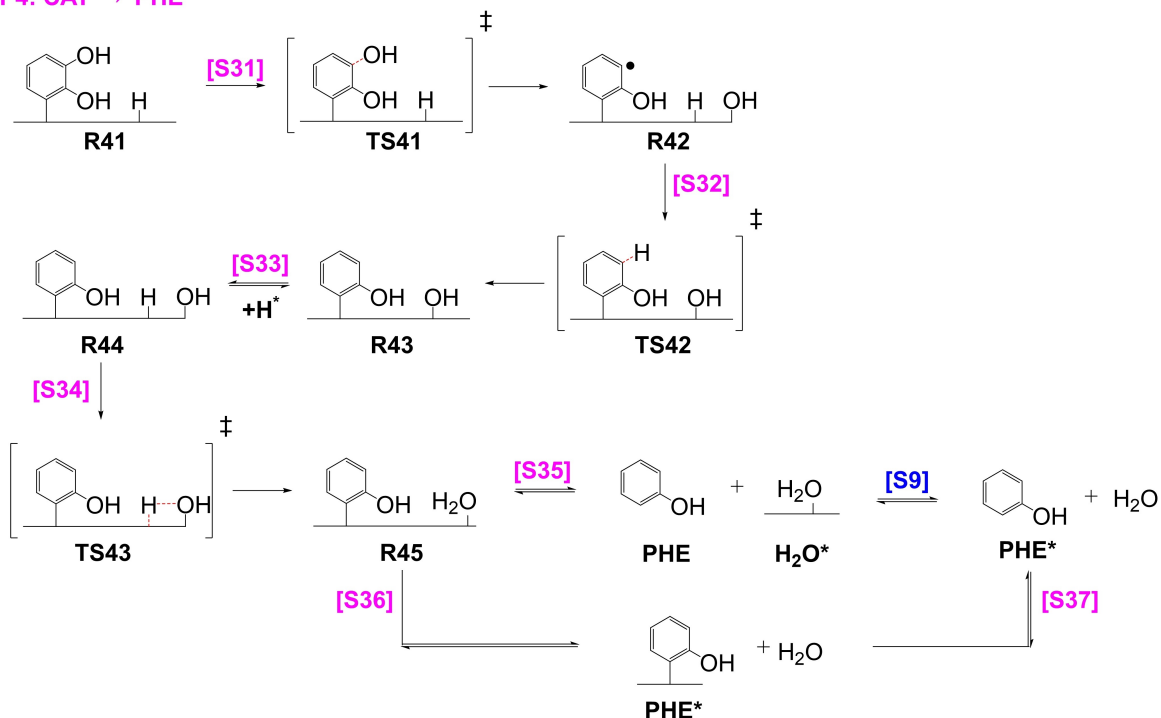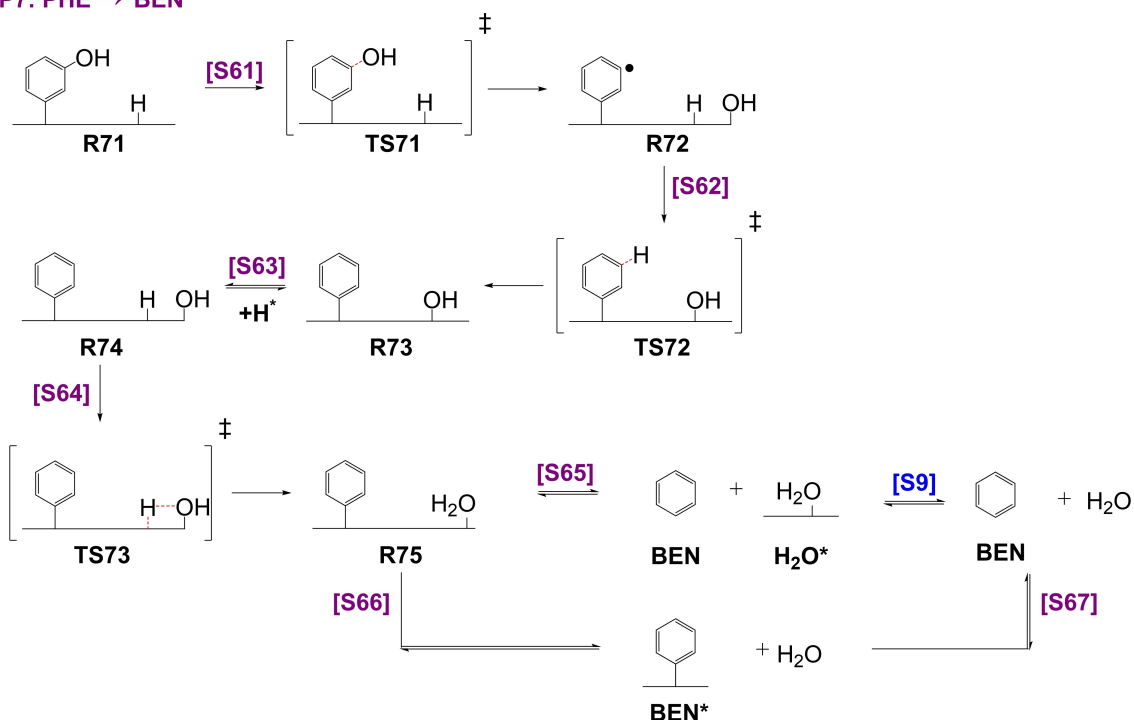
Scheme 3. The elementary steps of dehydroxylation of catechol to phenol (**P4**, pink) and of phenol to benzene (**P7**, purple). Desorption of water from an otherwise naked surface, **S9**, is an available step in both pathways, and was calculated identically to the desorption step in **P1**.

much higher for Ni(111), which is six orders of magnitudes higher than the rate constant for Co(0001). Pt(111) and Pd(111) have relatively high rate constants for this step, but much lower rate constants for deoxygenation. These results agree with previous studies on HDO reactions, where Pt and Pd catalysis showed favorable kinetics for the phenol hydrogenation steps.[47,48]

ChemCatChem

Research Article
doi.org/10.1002/cctc.202300671

Chemistry
Europe
European Chemical
Societies Publishing

Figure 3. Activation free energies (ΔG_a) and reaction free energies (ΔG_r) of the elementary steps of the initial dehydroxylation to phenol (**P4**, pink) and the final dehydroxylation to benzene (**P7**, purple) over each metal surface at 573 K.
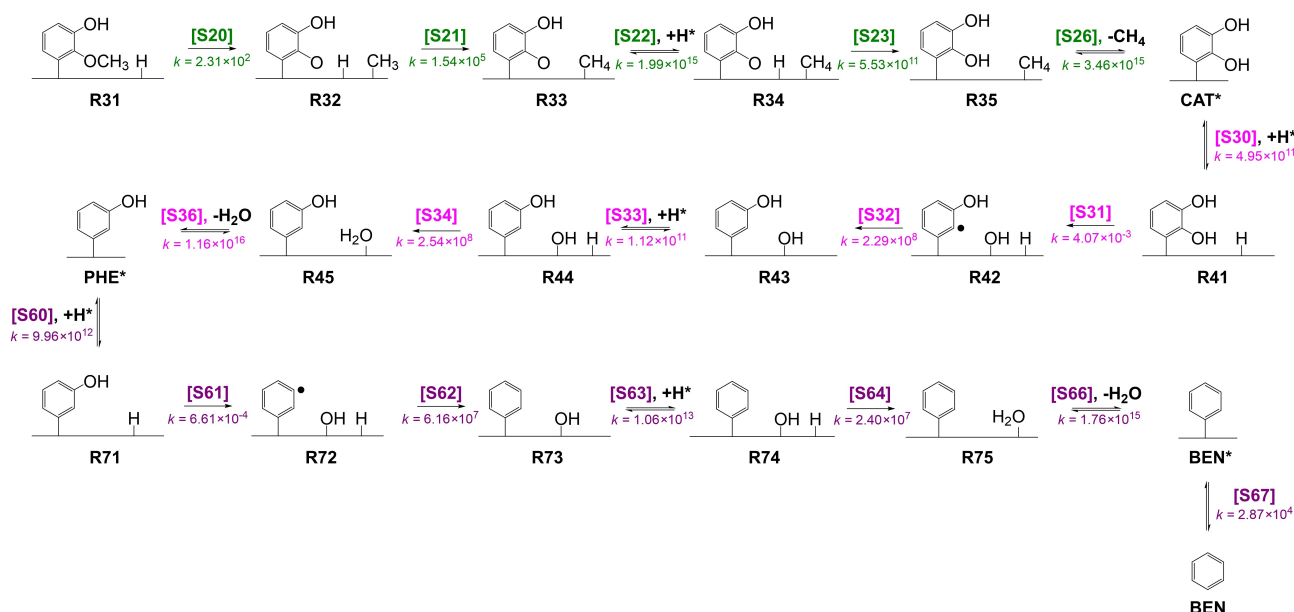
Scheme 4. The predicted mechanistic pathway for guaiacol HDO over Ni(111). Guaiacol is first demethylated to catechol (**P3**, green), which is then broken down into phenol (**P4**, pink) before undergoing a final hydrogenolysis to benzene (**P7**, purple). k in given in s^{-1} for first-order steps and $M^{-1} s^{-1}$ for second-order steps.

From the results of our calculations, we conclude that Ni(111) is the most favorable catalyst for guaiacol HDO at 573 K among the metals studied in this investigation, and that the most favorable mechanistic route is demethylation to catechol (**P3**), direct deoxygenation to phenol (**P4**), and a final dehydro-genation to benzene (**P7**). A complete schematic network of this pathway is given in Scheme 4. While more experimental data is needed to confirm our findings, preference for this mechanism has already been independently verified for Pt(111), where catechol production was shown to be four orders of

ChemCatChem

Research Article
doi.org/10.1002/cctc.202300671

Chemistry Europe
European Chemical
Societies Publishing

k, 573 K

	Co	Ni	Cu	Pd	Pt
S4	2.00E+00	6.41E-02	1.19E-04	2.20E-04	3.10E-04
S5	3.18E+04	2.43E+10	2.78E+13	8.49E+10	7.18E+09
S7	2.06E+02	6.11E+05	7.37E+06	5.44E+08	1.93E+10
S12	1.06E+01	8.41E-02	1.01E-05	3.24E-03	8.24E-04
S13	7.16E+09	3.87E+11	3.54E+06	1.34E+07	8.78E+09
S15	1.55E+04	1.54E+06	7.66E+04	3.21E+08	6.59E+10
S20	1.42E+04	1.54E+05	2.44E+05	5.93E+03	1.03E+08
S21	7.95E+14	1.99E+15	1.69E+12	1.84E+13	1.14E+15
S23	1.06E+08	6.43E+06	9.59E+09	1.14E+06	5.74E+02

k, 573 K

	Co	Ni	Cu	Pd	Pt
S31	9.22E+01	4.07E-03	3.57E-03	1.77E-05	1.89E-05
S32	4.10E+11	2.29E+08	5.08E+08	1.54E+06	3.89E+08
S34	8.98E-01	2.54E+08	2.04E+05	1.65E+07	3.44E+11
S61	6.49E+02	6.61E-04	7.48E-05	1.14E-05	1.06E-07
S62	8.51E+01	6.16E+07	4.86E+07	1.58E+09	4.73E+11
S64	1.54E+03	2.40E+07	6.69E+03	5.91E+07	9.66E+10

Figure 4. Calculated rate constants (k) at 573 K for the rate-determining steps of **P1** (blue), **P2** (red), **P3** (green), **P4** (pink), and **P7** (purple). k is given in s^{-1} for first-order steps and $M^{-1}s^{-1}$ for second-order steps.

magnitude faster than the direct production of phenol from guaiacol.[46] Another potential avenue for future research on HDO catalysis is the implementation of Ni in alloys and mixed metal nanoparticles. For instance, the hydrodeoxygenation of guaiacol,[49,50] catechol,[51] phenol,[52,53] and cresol[54] with bimetallic Ni–Fe catalysts has already shown promising experimental results, largely due to synergistic effects between metallic Ni and Ni–Fe alloy sites.[55] Additionally, in 2021, researchers at Kyung Hee University[56] were granted a patent for a bimetallic NiMo/Al$_2$O$_3$-TiO$_2$ catalyst for guaiacol HDO, which reportedly shows high selectivity towards cyclohexane, methylcyclohexane, and toluene. While a thorough investigation of the properties of mixed metal catalysts is beyond the scope of this work, it is likely that the synergistic effects between Ni and other metals in the d-block could be further exploited by synthetic chemists to promote new catalytic pathways.

Conclusions

We employed first-principles microkinetic modelling to simulate the hydrodeoxygenation of guaiacol to benzene over Co(0001), Ni(111), Cu(111), Pd(111), and Pt(111). We performed systematic and detailed analyses of the thermochemistry and kinetics to show that Ni(111) and Co(0001) are the most promising candidates for guaiacol HDO catalysis. Ni(111) exhibits a preferential reaction pathway combining demethylation, direct deoxygenation, and dehydrogenation to benzene, with exceptionally favorable kinetics for both deoxygenation and hydrogenation steps at 573 K. Meanwhile, Pd(111) and Pt(111) shows poor deoxygenation activity and slow cleavage of hydroxyl and methoxy groups from the central ring system. These results provide key understanding of the mechanistic chemistry behind guaiacol HDO, and we hope that our work will inspire the design of more effective catalysts for this strategic process.

Acknowledgements

Conflict of Interests

The authors declare no conflict of interest.

Data Availability Statement

The data that support the findings of this study are openly available in Converis at https://doi.org/10.17035/d.2023. 0259606156, reference number 259606156.
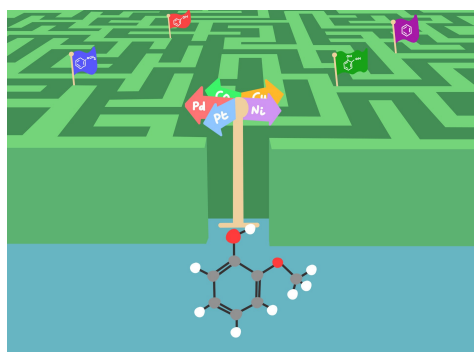
[1] R. W. Bentley, *Energy Policy* **2002**, *30*, 189–205.
[2] P. M. Mortensen, J.-D. Grunwaldt, P. A. Jensen, K. G. Knudsen, A. D. Jensen, *Appl. Catal. A* **2011**, *407*, 1–19.
[3] B. Zhang, D. Seddon, *Hydroprocessing Catalysts and Processes: The Challenges For Biofuels Production*, World Scientific, **2018**, vol. 17.
[4] E. Furimsky, *Appl. Catal. A* **2000**, *199*, 147–190.
[5] H. Shafaghat, J. Jae, Y.-K. Park, *Chem. Eng. J.* **2021**, *404*, 126531.
[6] X. Xu, C. Zhang, Y. Liu, Y. Zhai, R. Zhang, *Chemosphere* **2013**, *93*, 652–660.
[7] F. Morteo-Flores, A. Roldan, *Front. Catal.* **2022**, *2*, 1–12.
[8] D. Laurenti, P. Afanasiev, C. Geantet, *Appl. Catal. B* **2011**, *101*, 239–245.
[9] M. V. Bykova, D. Y. Ermakov, V. V. Kaichev, O. A. Bulavchenko, A. A. Saraev, M. Y. Lebedev, V. A. Yakovlev, *Appl. Catal. B* **2012**, *113*, 296–307.
[10] X. Zhang, T. Wang, L. Ma, Q. Zhang, Y. Yu, Q. Liu, *Catal. Commun.* **2013**, *33*, 15–19.
[11] H. Lee, H. Kim, M. J. Yu, C. H. Ko, J.-K. Jeon, J. Jae, S. H. Park, S.-C. Jung, Y.-K. Park, *Sci. Rep.* **2016**, *6*, 1–8.
[12] M. I. Campos-Franzani, N. F. Gajardo-Parra, C. Pazo-Carballo, P. Aravena, R. Santiago, J. Palomar, N. Escalona, R. I. Canales, *Fuel* **2020**, *280*, 118405.
[13] A. Bjelić, M. Grilc, B. Likozar, *Chem. Eng. J.* **2018**, *333*, 240–259.
[14] T. Nimmanwudipong, R. C. Runnebaum, D. E. Block, B. C. Gates, *Energy Fuels* **2011**, *25*, 3417–3427.
[15] D. Gao, Y. Xiao, A. Varma, *Ind. Eng. Chem. Res.* **2015**, *54*, 10638–10644.
[16] A. Bjelić, M. Grilc, M. Huš, B. Likozar, *Chem. Eng. J.* **2019**, *359*, 305–320.
[17] J. Hafner, G. Kresse, *Prop. Complex Inorg. Solids* **1997**, *140*, 69–82.
[18] G. Kresse, D. Joubert, *Phys. Rev. B: Condens. Matter Mater. Phys.* **1999**, *59*, 1758–1775.
[19] B. Hammer, L. B. Hansen, J. K. Nørskov, *Phys. Rev. B: Condens. Matter Mater. Phys.* **1999**, *59*, 7413–7421.
[20] S. Grimme, J. Antony, S. Ehrlich, H. Krieg, *J. Chem. Phys.* **2010**, DOI:10.1063/1.3382344.
[21] H. J. Monkhorst, J. D. Pack, *Phys. Rev. B* **1976**, *13*, 5188–5192.
[22] M. Methfessel, A. T. Paxton, *Phys. Rev. B* **1989**, *40*, 3616–3621.
[23] G. Henkelman, B. P. Uberuaga, H. Jónsson, *J. Chem. Phys.* **2000**, *113*, 9901–9904.
[24] J. W. Niemantsverdriet, I. Chorkendorff, *Concepts of Modern Catalysis and Kinetics*, John Wiley & Sons, **2006**.
[25] X. Lu, A. Roldan, *J. Phys. Chem. C* **2021**, *125*, 15950–15958.
[26] X. Lu, J. Zhang, W. K. Chen, A. Roldan, *Nanoscale Adv.* **2021**, *3*, 1624–1632.
[27] K. Agrawal, A. Roldan, N. Kishore, A. J. Logsdail, *Catal. Today* **2022**, *384–386*, 197–208.
[28] S. Francis, A. Boucher, G. Jones, A. Roldan, *Appl. Surf. Sci.* **2022**, *572*, 151317.
[29] H. Eyring, *J. Chem. Phys.* **1935**, *3*, 63–71.
[30] A. Roldan, Roldan Group: Kinetics, https://github.com/Roldan-Group/Kinetics.
[31] K. Agrawal, A. Roldan, N. Kishore, A. J. Logsdail, *Catal. Sci. Technol.* **2022**, *12*, 843–854.
[32] K. W. Kolasinski, *Surface Science: Foundations of Catalysis and Nanoscience*, John Wiley & Sons, 2nd edn., **2012**.
[33] F. E. Massoth, P. Politzer, M. C. Concha, J. S. Murray, J. Jakowski, J. Simons, *J. Phys. Chem. B* **2006**, *110*, 14283–14291.
[34] S. M. Wetterer, PhD thesis, Princeton University, **1998**.
[35] F. Morteo-Flores, A. Roldan, *ChemPhysChem* **2022**, *23*, e202100583.
[36] S. J. Carey, W. Zhao, Z. Mao, C. T. Campbell, *J. Phys. Chem. C* **2018**, *123*, 7627–7632.
[37] T. Mochizuki, S.-Y. Chen, M. Toba, Y. Yoshimura, *Appl. Catal. B* **2014**, *146*, 237–243.
[38] D. Gao, C. Schweitzer, H. T. Hwang, A. Varma, *Ind. Eng. Chem. Res.* **2014**, *53*, 18658–18667.
[39] J. Bredenberg, M. Huuska, J. Räty, M. Korpio, *J. Catal.* **1982**, *77*, 242–247.
[40] J. Chang, T. Danuthai, S. Dewiyanti, C. Wang, A. Borgna, *ChemCatChem* **2013**, *5*, 3041–3049.
[41] J. Wildschut, F. H. Mahfud, R. H. Venderbosch, H. J. Heeres, *Ind. Eng. Chem. Res.* **2009**, *48*, 10324–10334.
[42] J. E. Peters, J. R. Carpenter, D. C. Dayton, *Energy Fuels* **2015**, *29*, 909–916.
[43] A. B. Anton, D. C. Cadogan, *Surf. Sci.* **1990**, *239*, L458–L560.
[44] E. M. Karp, C. T. Campbell, F. Studt, F. Abild-Pedersen, J. K. Norskov, *J. Phys. Chem. C* **2012**, *116*, 25772–25776.
[45] M. G. Evans, M. Polanyi, *Trans. Faraday Soc.* **1936**, *32*, 1333–1360.
[46] A. Gutierrez, R. K. Kaila, M. L. Honkela, R. Slioor, A. O. I. Krause, *Catal. Today* **2009**, *147*, 239–246.
[47] A. M. Verma, N. Kishore, *Phys. Chem. Chem. Phys.* **2017**, *19*, 25582–25597.
[48] J. Lu, S. Behtash, O. Mamun, A. Heyden, *ACS Catal.* **2015**, *5*, 2423–2435.
[49] J. Zhou, W. An, Z. Wang, X. Jia, *Catal. Sci. Technol.* **2019**, *9*, 4314–4326.
[50] X. Liu, W. An, Y. Wang, C. H. Turner, D. E. Resasco, *Catal. Sci. Technol.* **2018**, *8*, 2146–2158.
[51] J. Zhou, W. An, *Catal. Sci. Technol.* **2020**, *10*, 6849–6859.
[52] D. M. Alonso, S. G. Wettstein, J. A. Dumesic, *Chem. Soc. Rev.* **2012**, *41*, 8075–8098.
[53] W. An, R. Zuo, J. Zhou, Q. Huang, C. Fang, *J. Phys. Chem. C* **2020**, *124*, 28052–28060.
[54] X. Liu, W. An, C. H. Turner, D. E. Resasco, *J. Catal.* **2018**, *359*, 272–286.
[55] Q. Han, M. U. Rehman, J. Wang, A. Rykov, O. Y. Gutiérrez, Y. Zhao, S. Wang, X. Ma, J. A. Lercher, *Appl. Catal. B* **2019**, *253*, 348–358.
[56] E. Y. Lee, P. D. Phan, *Catalyst For Hydrodeoxygenation of Guaiacol and Method for Selective Production of Hydrocarbon Compounds from Guaiacol*, KR102283321B1, **2021**.

RESEARCH ARTICLE

Dr. F. Morteo-Flores, M. Quayle, Dr. A. Salom-Català, Prof. M. Pera-Titus, Dr. A. R. Martinez*

1 – 12

First-Principles Microkinetic Study of the Catalytic Hydrodeoxygenation of Guaiacol on Transition Metal Surfaces

Catalytic Hydrodeoxygenation of Guaiacol: By constructing a first-principles microkinetic model from over 300 DFT models of the intermediates, we report that guaiacol HDO exhibits highly desirable deoxygenation and hydrogenation kinetics over Ni(111) at industrial temperatures.